ECS | The Electrochemical Society
Advancing solid state & electrochemical science & technology

Electrolyte Dependency on Ca^{2+} Insertion and Extraction Properties of V$_2$O$_5$

View the article online for updates and enhancements.

Electrolyte Dependency on Ca²⁺ Insertion and Extraction Properties of V₂O₅

Yoshiaki Murata,[z] Ryoji Inada,[*] and Yoji Sakurai[*,z]

Department of Electrical and Electronic Information Engineering, Toyohashi University of Technology, Tempaku, Toyohashi, Aichi 441-8580, Japan

The influence of the electrolyte structure on the Ca²⁺ ion insertion and extraction properties of V₂O₅ was studied by changing the electrolyte concentration or solvent. The electrolyte structure was analyzed by Raman spectroscopy. The most significant changes were found in the molar ratio of the contact ion pair (CIP) in the total ionic species. Among the various electrolytes, 0.3 M Ca(TFSI)₂ dissolved in ethylene carbonate and dimethyl carbonate (0.3 M EC:DMC) and 0.5 M Ca(TFSI)₂ dissolved in triglyme (0.5 M G3) have relatively small molar ratios of CIPs. The electrochemical performance was strongly related to the molar ratio of the CIPs. A high coulombic efficiency and high capacity were observed when using 0.3 M EC–DMC. Moreover, 0.5 M G3 showed the highest capacity despite its low coulombic efficiency. This could be related to the formation of solvent-separated ion pairs (SSIPs) due to the low polarity of G3 and its solvation form that encapsulates Ca²⁺. SSIPs had a reductively unstable character as that of the CIPs. Surface analysis revealed that the thinner the surface film produced, the lower the CIP content. This was deemed responsible for the rate performance enhancements, given the potential electrochemical instability of the Ca-containing CIPs.

Recently, the demand for secondary batteries has increased. In particular, lithium-ion batteries (LIBs) are often used in a wide range of applications, such as mobile equipment and electric vehicles (EVs), because of their high energy density. However, the current capacity, safety, and cost reduction of LIBs are insufficient. Therefore, multi-valent-ion batteries have attracted attention as post-LIBs because of their high energy density, high safety, and low costs compared with those of the LIBs. Among them, calcium-ion batteries (CIBs) have some advantages, such as their relatively high cell voltage (due to the low standard electrode potential of Ca/Ca²⁺ [−2.87 V vs NHE], which is comparable with that of Li/Li⁺ [−3.05 V vs NHE]), and their relatively high diffusion rate in electrode materials owing to the low charge density of Ca²⁺ compared with those of other multivalent ions.[1] As electrode materials for CIBs, α-V₂O₅,[2,3] HTB–FeF₃·0.33H₂O,[4] layered NaₓFePO₄F,[5] Prussian blue analogs (PBAs),[6–10] TiS₂,[11] Sn,[10,12] graphite,[13] and Ca metal[1,14,15] have been studied, and the number of relevant reports is increasing rapidly. In particular, in anode materials, a fairly high rate-performance has been reported,[1,10,12–15] and great progress has been made toward practical use. However, the rate and cycling performance of the cathode materials in Ca-based organic electrolytes are poor compared to those of the LIBs. This poor electrochemical performance can be attributed to several factors. First, electrode materials have low Ca²⁺ conductivity because of the large charge density of Ca²⁺. This can be solved using the crystal structures that have relatively high ionic conductivity, such as open-framework-type structures, and/or by reducing the grain size of the electrode material, which will reduce the ionic diffusion path.[4] Another factor is the large electrode/electrolyte charge transfer resistance. Depending on the type of electrolyte, the electrochemical stability, composition, and thickness of the surface film change, significantly affecting the electrochemical performance. Recently, electrolytes that can dissolve and deposit Ca metals and possess good oxidation stability are developed for CIBs. For example, calcium tetrafluoroborate dissolved in ethylene carbonate and propylene carbonate (Ca(BF₄)₂/EC–PC)[1] and calcium tetrakis(hexafluoroisopropyloxy)borate dissolved in monoglyme (Ca[B(hfip)₄]₂/G1).[14,15] However, their coulombic efficiency was less than 90%. The use of Ca(BF₄)₂/EC–PC

requires a high temperature for operation and produces a large amount of CaF₂ as a by-product of an unknown origin. Further investigation of many unresolved reactions is required to improve the electrochemical performance of CIBs. From another perspective, a large difference in the overvoltage of PBAs is observed when aqueous electrolytes and organic electrolytes are used.[16] In this regard, we previously reported that the presence of water in the electrolyte dramatically improves the electrochemical performance of V₂O₅ cathodes. This phenomenon is caused by changes in the solvation structure and salt dissociation state.[3] For practical applications, it is preferable to design an electrolyte that does not contain water and has an excellent electrolyte structure that improves the electrochemical performance.

In this study, we analyzed the electrolyte structure with changes in solvent species and salt concentration and found a combination that improved the electrochemical performance of the cathode material. We used V₂O₅ as the cathode material, and to considerably eliminate the effect of ion diffusion in the solid phase, we adopted V₂O₅ nanosheets, which have a sufficiently short ionic diffusion path.

Experimental

V₂O₅ nanosheets were synthesized by the heat treatment of NH₄V₄O₁₀ nanosheets synthesized by a hydrothermal method.[17] For the synthesis of the V₂O₅ nanosheets, 0.85 g of ammonium metavanadate (NH₄VO₃) and 0.65 g of oxalic acid (H₂C₂O₄) were dissolved in 32.5 ml of deionized water and stirred overnight under room temperature. After stirring, the solution was transferred into a 45 ml Teflon-lined autoclave and maintained at 180 °C for 24 h. The obtained powder was rinsed with distilled water and dried overnight at 80 °C under a vacuum. Finally, the synthesized sample was immediately placed in a muffle furnace at 400 °C for 1 h, and the V₂O₅ nanosheets were obtained.

The crystal structure of the resultant sample was characterized by X-ray diffraction (XRD). XRD measurements were performed using an X-ray diffractometer (RINT 2550, Rigaku). The XRD patterns were recorded at an angular range, 2θ, from 10° to 120° with a Cu-Kα source set at 40 kV and 200 mA. The morphology was characterized by field emission scanning electron microscopy (FE–SEM, SU800, Hitachi High-Tech) and transmission electron microscopy (TEM, JEM-1400 Plus, JEOL).

The electrolytes were prepared by dissolving calcium bis(trifluoromethanesulfonyl)imide (Ca(TFSI)₂, Solvay) in an organic solvent at

*Electrochemical Society Member.
[z]E-mail: murata@cec.ee.tut.ac.jp; sakurai@ee.tut.ac.jp

a concentration of 0.2–0.5 M. For the organic solvent, a 50:50 vol.% mixture of EC and PC (EC:PC, Kishida) or a 50:50 vol.% mixture of EC and dimethyl carbonate (EC:DMC, Kishida), PC (Kishida), G1 (Kanto), triglyme (G3, Kanto), or acetonitrile (AN, Kishida) was used. The salt was vacuum dried at 150 °C for 12 h before use. The water content in the electrolytes, as measured by Karl Fischer titration, was lower than 50 ppm.

In the following section, the electrolyte samples are described using salt concentration and solvent species (e.g., 0.5 M EC:DMC).

The pairing states of Ca^{2+} and $TFSI^-$ anions were analyzed by Raman spectroscopy, which was performed using a Raman spectrometer (NSR-7100, JASCO). Each electrolyte was sealed in a transparent moisture barrier film (GX-film, Toppan) inside an Ar-filled glove box, and the Raman spectra were measured through the film.

The electrochemical behavior of the V_2O_5 nanosheets in the various electrolytes was characterized by galvanostatic cycling tests. The electrochemical measurements were conducted in a three-electrode beaker-type cell with V_2O_5 composite electrodes as the working electrodes, an Ag wire as the quasi-reference electrode, and a porous activated carbon electrode as the counter electrode. The cell assembly was conducted in an Ar-filled glove box, and the cell was sealed using a sealing tape to prevent volatilization of the electrolyte. The working electrode slurries were composed of 70 wt.% of the active material, 20 wt.% of acetylene black (AB, Denka), and 10 wt.% of polyvinylidene difluoride (PVdF, Kureha) dissolved in N-methyl-2-pyrrolidinone (NMP, Kishida). The obtained slurries were coated onto a carbon-coated titanium foil and vacuum-dried

overnight at 120 °C. The dried electrode was punched into a circular disk with a diameter of 14 mm, a part of the electrode was peeled off, and the titanium wire was welded to make the working electrodes. Counter electrodes were prepared by compressing a mixture of 80 wt.% of activated carbon (AP11-0010, ATEC), 10 wt.% of AB, and 10 wt.% of polytetrafluoroethylene (PTFE, Polyflon™ F-104, Daikin). A titanium mesh was used as the current collector for the counter electrodes. The mass loadings of the working and counter electrodes were 3 mg cm^{-2} and 75 mg cm^{-2}, respectively.

All cells were allowed to rest for 12 h before testing. The galvanostatic cycling tests were performed at a maintained temperature of 30 °C and a current density of 0.05–1C (1C = 147.35 mA g^{-1}) using a battery charge/discharge system (SM8, Hokuto). The coulombic efficiency was calculated as the charge (Ca^{2+} extraction) capacity/discharge (Ca^{2+} insertion) capacity.

The potential range of the cycling tests was set to −1.5–1 V vs the Ag quasi-reference electrode in 0.5 M EC:DMC. The potential shift of the Ag quasi-reference electrode depended on the electrolyte type, and it was corrected by the potential difference with the metallic Li measured in another container. To prevent Li contamination, we avoided the interaction between Li and the electrolyte of the measuring cells.

In the following statements, all potential values are corrected to the potential of the Ag quasi-reference electrode in 0.5 M EC:DMC.

The elemental analysis of the electrodes after the rate performance test was conducted by X-ray photoelectron spectroscopy (XPS, Quantera SXM-CI, ULVAC-PHI). The XPS spectra were recorded with an Al-Kα source, and a depth analysis was performed by etching using Ar$^+$ sputtering. The analysis was performed on samples that were charged (Ca^{2+} extracted) after the cycle and rate performance tests, and they were thoroughly rinsed with DMC before the analysis.

Results and Discussion

The XRD pattern of the synthesized sample is shown in Fig. 1. The sample was perfectly indexed to the orthorhombic α-V_2O_5 phase (JCPDS No. 01-072-0433), and no other impurities were detected. The peak intensity at approximately 20.3°, corresponding to the (001) plane, was higher than that of the PDF card. Therefore, the V_2O_5 nanosheets were oriented along the c-axis direction. The FE-SEM and TEM images (Fig. 2) showed that the sample had a sheet shape and width of 100–300 nm. The FE-SEM image indicates that the thickness is approximately 20 nm or less.

Figure 3 shows the structural analysis results of the electrolytes, which were examined using Raman spectroscopy. A comparison of
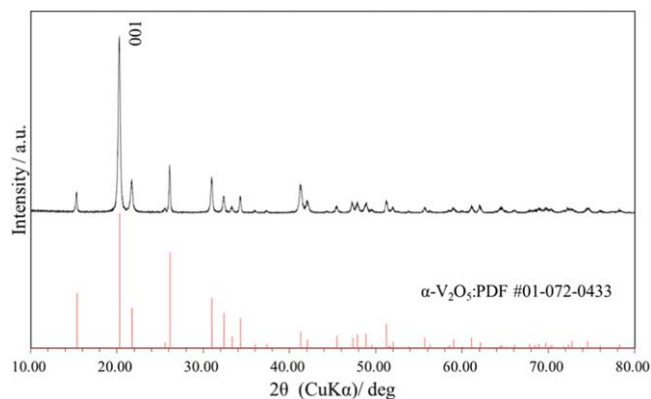

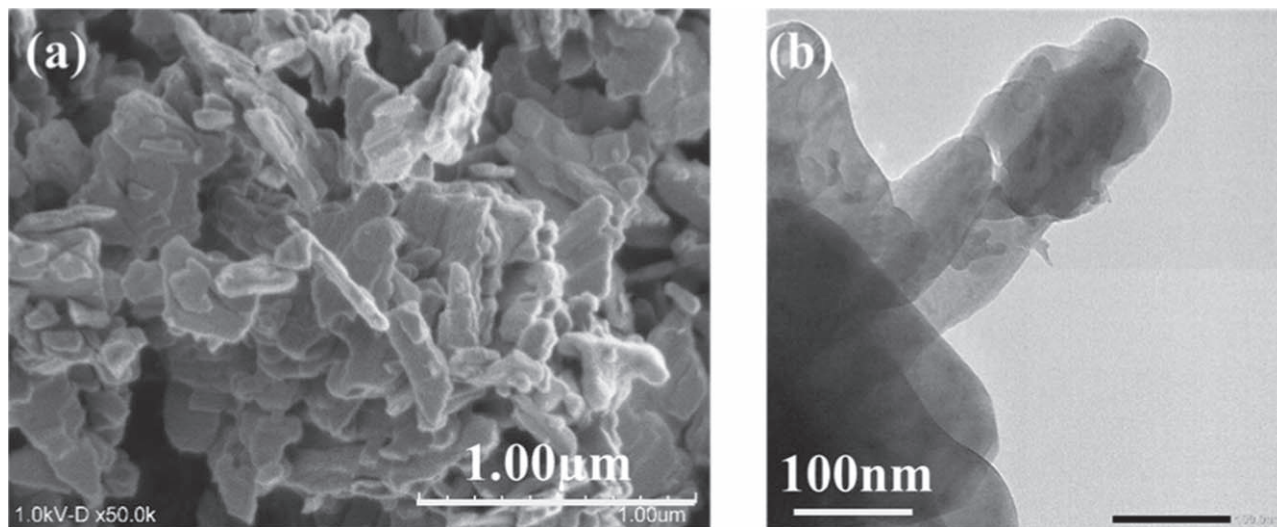**Figure 1.** Observed XRD pattern of the synthesized V_2O_5 nanosheets.

Figure 2. (a) FE–SEM image and (b) TEM image of the synthesized V_2O_5 nanosheets.
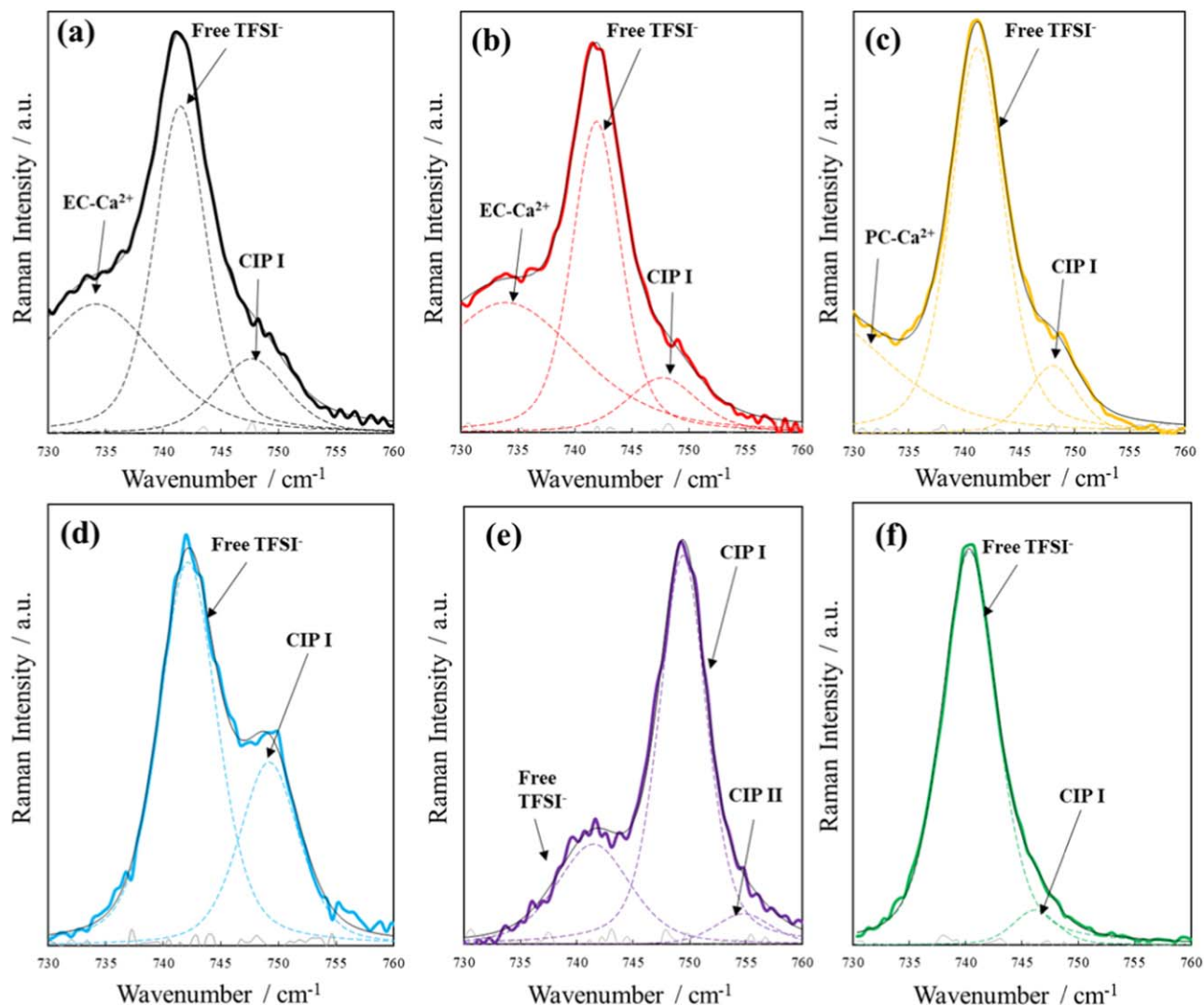
Figure 3. Raman spectra of the electrolytes: TFSI$^-$ region (a) 0.5 M EC:DMC, (b) 0.5 M EC:PC, (c) 0.5 M PC, (d) 0.5 M AN, (e) 0.25 M G1, and (f) 0.5 M G3.

the structure was performed at a concentration of 0.5 M. G1 was analyzed at a concentration of 0.25 M, which is close to the saturation concentration. The peak of the S–N–S stretching mode of TFSI$^-$ was observed at approximately 740–755 cm^{-1}. The position of this peak changes according to the coordination state of the cations around TFSI$^-$.[18] In our Ca-based electrolyte, a dissociated TFSI$^-$ (denoted as Free TFSI$^-$) at 742 cm^{-1}, one TFSI$^-$ paired with Ca^{2+} (CaTFSI$^+$: contact ion pair I, denoted as CIP I) at 748 cm^{-1}, and two or more TFSI$^-$ paired with Ca^{2+} (Ca(TFSI)$_n^{-(n-2)}$: contact ion pair II, denoted as CIP II) at 755 cm^{-1} were confirmed. For 0.5 M G3, the peak around 740 cm^{-1} was on a lower wavenumber side than for the other electrolytes, suggesting the formation of solvent-separated ion pairs (SSIPs).[19] However, we cannot distinguish between SSIPs and free TFSI$^-$ under our measurement conditions. CIP II was observed only when G1 was used, suggesting that G1 has a particularly low salt dissociation ability. This also corresponds to the low solubility of the Ca(TFSI)$_2$ salt in G1.

When discussing the exact quantification, it is necessary to discuss the Raman scattering coefficient for each peak (Free TFSI$^-$ and CIPs), but unfortunately, this information could not be found in the previous literature. In the previous study, the molar scattering coefficients of TFSI$^-$ and Mg^{2+}-TFSI$^-$ CIP were studied in Mg(TFSI)$_2$-based ionic liquids.[20] In this study, the ratio of the molar scattering coefficient of free TFSI$^-$ and Mg^{2+}-TFSI$^-$ CIP: J$_f$/J$_c$ was 0.9 ± 0.1, and it was concluded that the Raman scattering

coefficient was nearly identical even in the ionic liquid where the cation-anionic interaction was relatively strong. Since our research was evaluated in an organic solvent-based electrolyte and a Ca-based system with a slightly smaller cation-anionic interaction than the Mg-based ionic liquid system, the molar scattering coefficient of Ca^{2+}-TFSI$^-$ CIP can be regarded as approximately the same or
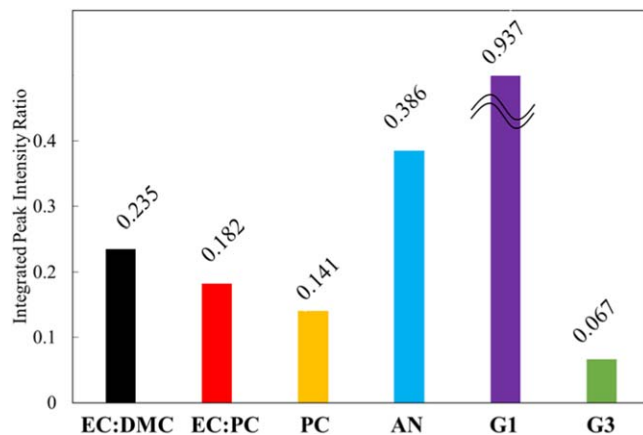

Figure 4. The integrated peak intensity ratio of CIP to total TFSI$^-$.
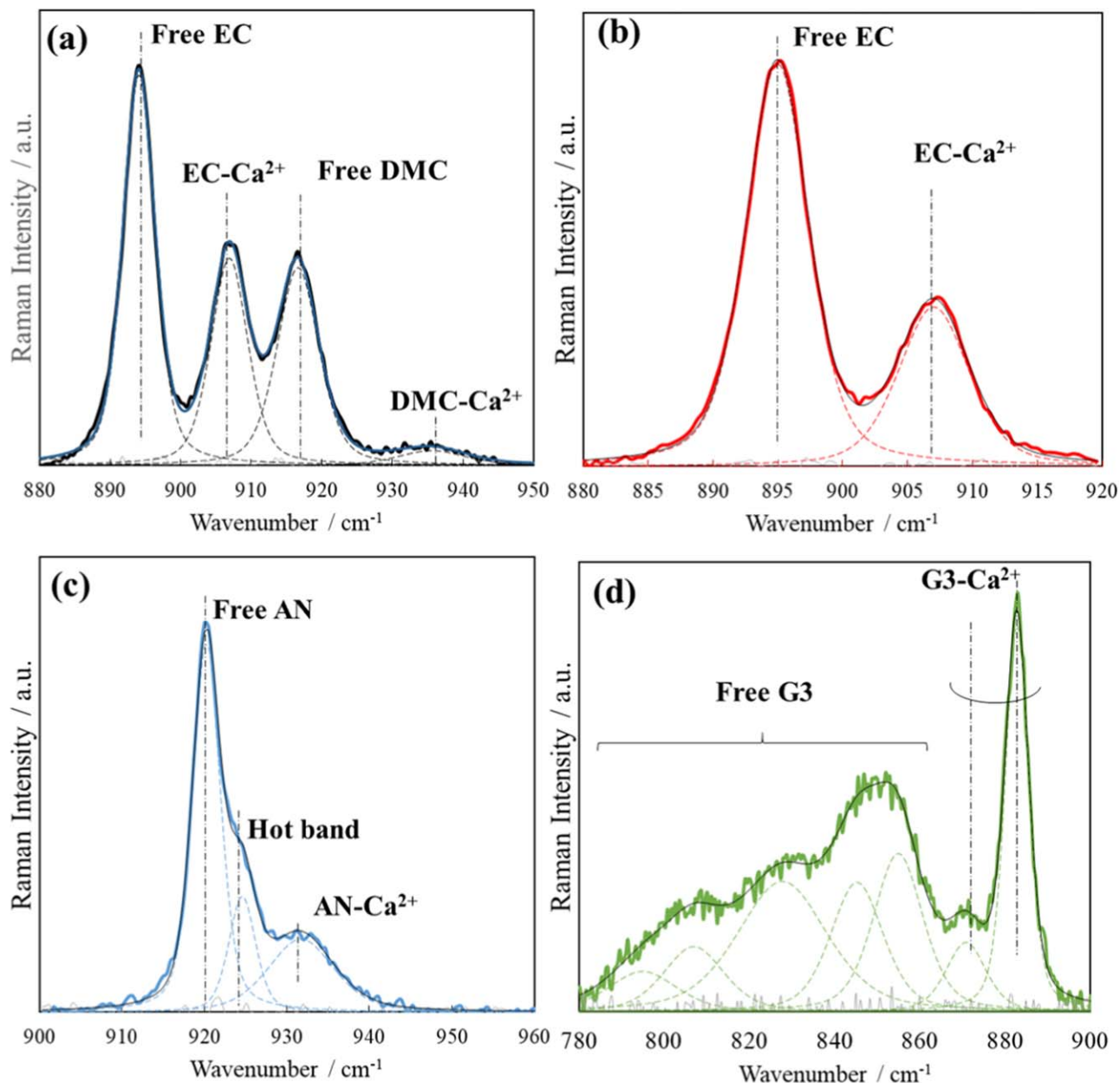
Figure 5. Raman spectra of the electrolytes: solvent region (a) 0.5 M EC:DMC, (b) 0.5 M EC:PC, (c) 0.5 M AN, and (d) 0.5 M G3.

Table I. Average solvation number in each electrolyte.

Electrolyte		Average solvation number
0.5 M EC:DMC	EC	3.56
	DMC	0.85
0.5 M EC:PC	EC	2.91
	PC	—
0.5 M AN		7.69
0.5 M G3		1.4

slightly smaller than that of free TFSI⁻. Conversely, the CIP-derived peaks in each electrolyte were observed at the same position, suggesting that the CIPs were in a similar state and had the same Raman scattering coefficient. Therefore, the ratio of the integrated peak intensity of the CIP peaks to the total TFSI⁻ peaks can be a semi-quantitative indicator of the degree of contact ion pairing. The
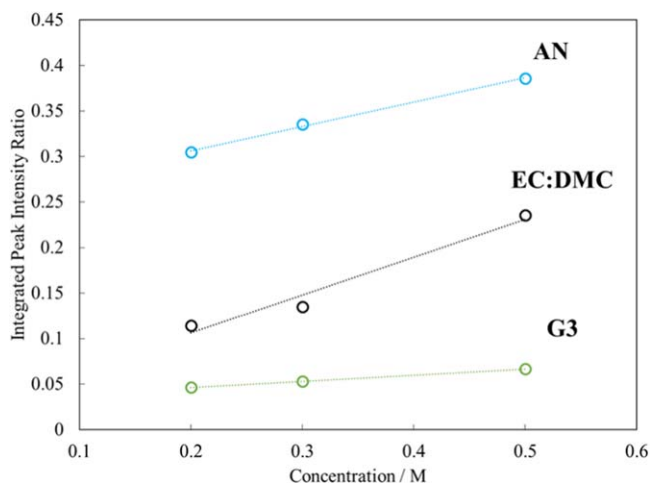
integrated peak intensity ratio of ion-paired TFSI⁻ with Ca^{2+} (CIPs) to the total TFSI⁻ was calculated and is shown in Fig. 4. The calculation was performed by dividing the total intensity of CIP I and CIP II by the total intensity of TFSI⁻. Thus, they are in the following order: G3 < PC < EC:PC < EC:DMC < AN < G1. A comparison of the solvents of EC:DMC and PC showed that PC had a relatively small contact ion-pairing ratio, and EC:PC had a slightly smaller contact ion-pairing ratio than EC:DMC. This is presumed to be due to the solvent species, which contribute to solvation.

The solvation structure was also analyzed by Raman spectroscopy. The analysis was performed for 0.5 M EC:DMC, 0.5 M EC:PC, 0.5 M AN, and 0.5 M G3. 0.5 M EC:PC was analyzed only for EC at independent positions because the PC peak was considerably close to the EC, making it difficult to separate. As shown in Figs. 5a, 5b, the peaks attributed to the ring bending mode of free EC and solvated EC[18] are found at approximately 890–910 cm⁻¹ for 0.5 M EC:DMC and 0.5 M EC:PC. Further, for EC:DMC, a peak attributed to the C–O stretching mode of free DMC and solvated DMC[21] appeared at approximately 910–950 cm⁻¹. This indicates that EC

Table II. Physical properties of the solvents.

Solvent	Dielectric Constant	Dipole Moment/D	Donor Number (DN)
EC	90.5[23] [a)]	4.81[23]	16.4[24]
PC	65.5[23]	5.36[23]	15.1[24]
DMC	3.20[25]	0.355[26]	17.2[24]
AN	35.9[27]	3.44[26]	14.1[24]
G1	7.55[28]	1.62[28]	24[29]
G3	7.62[28]	2.16[28]	14[29]

a) At 40 °C.

Figure 6. Electrolyte concentration dependence of the integrated peak intensity ratio of CIP to total TFSI⁻ with the electrolyte concentration.

and DMC contributed to the solvation. For 0.5 M AN, a peak attributed to the C–C stretching mode of free AN and solvated AN appeared at approximately 910–950 cm^{-1}, and a peak that cannot be attributed to these modes appeared at approximately 924 cm^{-1}, which is attributed to the hot band[22] (Fig. 5c). Finally, for 0.5 M G3, a peak attributed to the C–O stretching mode of G3 appeared at 780–900 cm^{-1} with free G3 and solvated G3 observed at approximately 780–860 cm^{-1} and 860–900 cm^{-1}, respectively[19] (Fig. 5d). It is known that the position of the peak of solvated G3 is dependent on the solvation structure. From the results of density-functional theory (DFT) calculations, it was found that several structures with similar peak positions and formation energies appeared, and it was difficult to separate them, but at least three structures were identified (Figs. S1 and S2 available online at stacks.iop.org/JES/168/020528/mmedia). Furthermore, the average solvation number was calculated using the formula below.[22] As mentioned above, the solvation number in 0.5 M EC:PC was calculated only for EC.

$$N = \frac{I_{\text{solvated}}}{I_{\text{solvent}}} \cdot \frac{C_{\text{solvent}}}{c_{Ca^{2+}}},$$

where N is the average solvation number, I_{solvated} is the integrated peak intensity from the solvated solvent, I_{solvent} is the total integrated peak intensity of the solvent, c_{solvent} is the concentration of the solvent, and $c_{Ca^{2+}}$ is the concentration of the Ca salt. Notably, in this study, this equation was approximated when the Raman scattering coefficients of the free and solvated solvents were assumed to be equivalent. Therefore, it can be used for intercomparison between the same solvents, but it does not provide the exact solvation number, and it is always underestimated. Notably, the coordination number was further underestimated for 0.5 M G3 because only the peaks near 882 cm^{-1} and 870 cm^{-1} observed by solvated G3 were used to calculate the solvation number. Further, we did not take into

account the solvated G3 peak that appeared at 780–850 cm^{-1} due to its weak Raman activity and difficult peak separation.

Table I shows that the solvation number of EC is slightly lower in EC:PC than in EC:DMC. This indicates that PC participates in the solvation shell even more than DMC in the EC:PC solvent. Certain solvents selectively solvate cations in mixed solvents, such as EC:DMC and EC:PC, and in both cases, EC preferentially solvates cations.[18] However, in both cases, the mixed co-solvent (DMC or PC) contributes to the solvation. A comparison of EC:PC and PC showed that PC had a relatively small contact ion-pairing ratio. Thus, PC had a higher salt dissociation ability than EC. EC:DMC had a higher ratio than the two other cases; this shows the low salt dissociation ability of DMC.

The salt dissociation ability of a solvent depends on its polarity. The dielectric constant and dipole moment are often used as parameters to represent the polarity of the solvents. The salt dissociation ability of a solvent with high polarity tends to be high, as shown by the comparison of EC, PC, and AN in Table II.

The fact that PC has a higher salt dissociation ability than EC, despite its low dielectric constant, suggests that the dipole moment may be dominant in the salt dissociation ability, but there is no confirmation. G3 has the highest salt dissociation ability despite its low dielectric constant and dipole moment, which sets it apart from the other solvents. Moreover, G1, which has similar parameters, has almost no salt dissociation ability. This suggests that the salt dissociation mechanism of G3 is different from that of the other solvents. G3 solvates to encapsulate the cation and cause salt dissociation by dividing the cation and anion (Fig. S1).[26] However, considering the small polarity of G3, there is a high possibility that it is not a complete dissociation but strictly an SSIP formation. The formation of SSIP requires a certain solvent molecular size, and CIP is likely to be formed in solvents with small molecular sizes and insufficient dipole moments, such as G1 and AN.

The electrolyte concentration dependence of the integrated peak intensity ratio of the CIP to total TFSI⁻ was examined for EC:DMC, G3, and AN (Fig. 6). The concentration dependence of the Raman spectra is also shown in Supplementary Fig. S3.4. A decrease in the peak intensity ratio with decreasing concentration was observed in all the electrolytes, which is due to the salt dissociation with decreasing concentrations. Interestingly, a strong concentration dependence was observed only when EC and DMC were used. This can be partly attributed to the changes in the solvation number. Table III shows the average solvation number for each concentration of the EC:DMC solvent. The total of average solvation number of

Table III. Electrolyte concentration dependence of the average solvation number in EC:DMC.

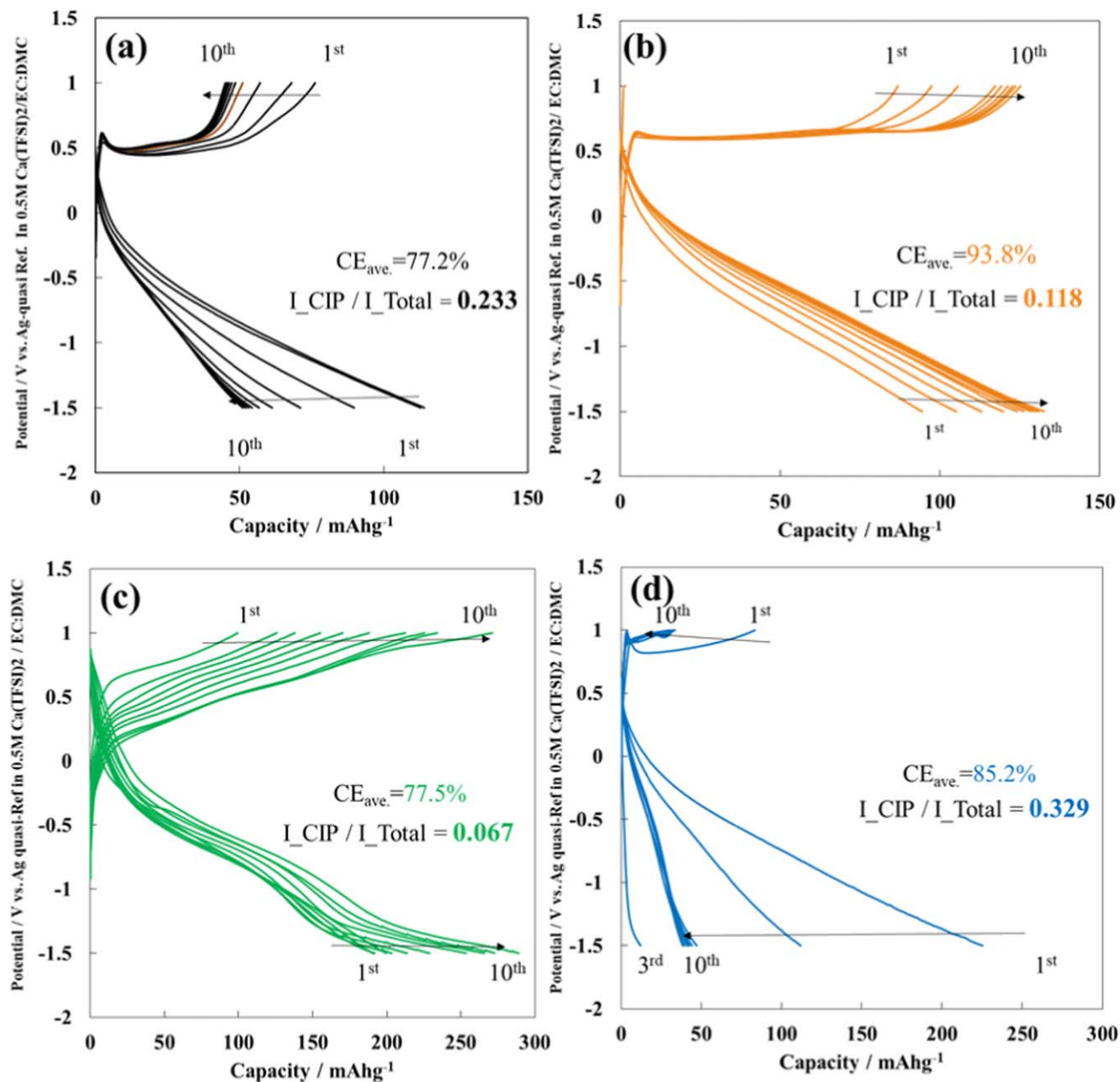| Solvent		Concentration [M]		
		0.20	0.30	0.50
EC:DMC	EC	5.18	4.66	3.56
	DMC	0.14	0.38	0.85

Figure 7. Galvanostatic cycling test curves of the V_2O_5 nanosheets in (a) 0.5 M EC:DMC, (b) 0.3 M EC:DMC, (c) 0.5 M G3, and (d) 0.5 M AN.

the EC and that of DMC decreases with increasing concentrations. This implies that the CIPs were produced. Furthermore, the ratio of the solvation number of the DMC gradually increased with increasing concentration, suggesting that the increase in the contribution of the DMC with a low salt dissociation ability to solvation as the concentration increases. In other words, the strong dependence of the CIP ratio on the concentration of EC:DMC was due to the change in the solvation state with the change in concentration.

Figures 7a–7d shows the results of the galvanostatic cycling tests, where 0.5 M EC:DMC, 0.3 M EC:DMC, 0.5 M G3, and 0.5 M AN were used. The Ca^{2+} extraction capacity in the first cycle was approximately 90 mAh g^{-1}, and the capacity was stabilized after 7–10 cycles. The capacity in the 10th cycle was better with relatively few CIPs. In particular, a high coulombic efficiency of 95% and high capacity of 133 mAh g^{-1} emerged at 0.05C when 0.3 M EC:DMC was used. When 0.5 M G3 was used, a high capacity of 289 mAh g^{-1} was observed, but the coulombic efficiency was only 78%. Additionally, the desolvation process was affected by different solvent species. It is known that solvation energy depends on the polarity of

the solvent.[30] A relatively low overvoltage was observed in G3 and for the first cycle only in AN, which had low polarity. However, the subsequent cycles showed the rapid degradation of AN, and the coulombic efficiency of G3 was low.

For 0.3 M EC:DMC and 0.5 M G3, the capacity gradually increased with the increasing number of cycles. This phenomenon was often observed when the full capacity of the active material was not obtained owing to the influence of overvoltage, and it has been confirmed in systems such as magnesium ion batteries.[31] Although the mechanism by which the overvoltage decreases is unclear, the utilization rate of the active material increased because of the crushing and deformation caused by cycle repetition. The activation process was not observed for 0.5 M EC:DMC and 0.5 M AN. In particular, the activation process may have occurred, but the capacity was much more severely degraded. Furthermore, the coulombic efficiency improved and stabilized after 7–10 cycles, regardless of the electrolyte used. This capacity degradation was caused by the formation of the passivation film due to the decomposition of the electrolyte. This surface film is effective for preventing excess side
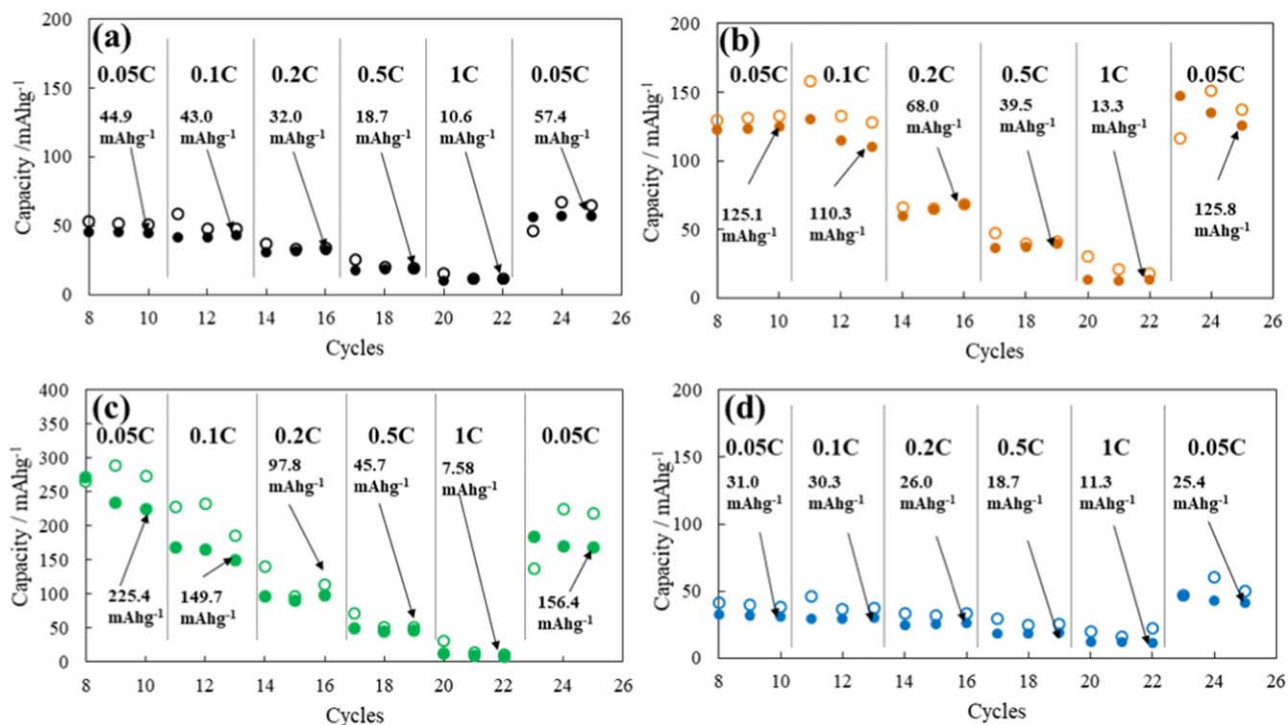
Figure 8. Charge/discharge capacities at different current densities of the V_2O_5 nanosheets. in (a) 0.5 M EC:DMC, (b) 0.3 M EC:DMC, (c) 0.5 M G3, and (d) 0.5 M AN. The open and closed circles indicate the discharge and charge capacities, respectively.

reactions, although there are differences in overvoltage, depending on the composition of the film. The severe degradation of two electrolytes that have a large ion CIP ratio (0.5 M EC:DMC and 0.5 M AN) agrees with the fact that CaTFSI[+] CIP is electrochemically unstable and a major decomposition specie in the electrolyte.[3] Moreover, the coulombic efficiency in the first to third cycles worsened as the CIPs increased. However, 0.5 M G3 had a relatively poor coulombic efficiency despite having the highest capacity. As a factor of the instability of the electrolyte when G3 is used, $Ca^{2+}(G3)_n$ TFSI[−] SSIP may also be as reductively unstable as CaTFSI[+] CIPs.

In the comparison of the 0.5 M EC:DMC and 0.3 M EC:DMC in the same solvent, a difference in the overvoltage was not observed in the first cycle. This implies that the salt dissociation energy of CIP is not considerably high and does not directly affect the overvoltage. However, the overvoltage is thought to be large because of the surface film produced by the decomposition of the CIPs.

These results suggest that there is a trade-off between the decrease in overvoltage caused by the decrease in the desolvation energy, the formation of electrochemically unstable SSIP/CIP for the polarity of the solvents, and it is necessary to achieve the right balance for high stability and high electrochemical performance.

Conversely, the potential overshoot was confirmed at the beginning of the extraction potential curves except for 0.5 M G3. Furthermore, the peak potential of the overshoot correlated with the molar ratio of CIPs. This overshoot occurred because of the passage or breakage of the formed passivation film. From this viewpoint, 0.5 M G3 showed no potential overshoot at the beginning of the extraction; thus, no film inhibited the electrochemical reaction. In other words, the chemical species produced by the decomposition of the CIP and decomposition of SSIP were fundamentally different.

Following the cycling test, the rate performance was measured for the same cells (Fig. 8). Considering the capacity trend confirmed in the cycling tests, the rate performance is better with relatively few CIPs. This result further suggests that the reduction in the negative effects of the CIP decomposition is more important than the reduction in desolvation energy. After the current density of 0.1C, the capacity difference between 0.3 M EC:DMC and 0.5 M G3 was

comparable, suggesting the rate-limiting effect of the solid phase diffusion in the V_2O_5 structure rather than in the desolvation processes. The coulombic efficiency improved at a current rate of 0.2C or higher. This indicates that the decomposition of CIP was kinetically slower than that of the Ca^{2+} insertion reaction.

The quantitative elemental analysis by XPS (Fig. 9) shows the atomic concentrations of the electrodes after the rate performance tests. Elemental analysis in the depth direction was performed by etching using Ar^{+}, and the concentrations were normalized using vanadium. In all the samples, the elements derived from CaTFSI[+] CIP, such as fluorine, sulfur, and calcium, were detected. As shown in the XPS spectra, the chemical species did not change significantly in any electrolyte, including the carbon environment. This suggests that most of the surface films comprised inorganic species (Figs. S5–S8). Although the chemical species inside the film are not always accurate because of the damage caused by Ar^{+} etching, CaF_2, CaS_xO_y, and CaS were observed as inorganic films. A comparison of the atomic concentrations between the surface and bulk of each sample revealed that the concentration of each element was relatively high near the surface. This is because the exposure of the active material is small near the surface and contains considerable information about the components of the surface film. Ca, S, and F remained in the samples etched for 20 min (200 nm vs SiO_2), and the amount did not change even after etching for 60 min (600 nm vs SiO_2) in any sample. Considering that the thickness of the active material particles was approximately 20 nm and the maximum etching amount was 600 nm vs SiO_2, it is also important to note that we etched all of the active material particles that were present on the outermost surface of the composite electrode. Further, we measured the underlying particles and their surface film. After etching for a while, the elemental ratios converged toward a certain value, and it is thought that the average information reflecting the overall film formation was collected in this experiment.

The information of the detected F also includes the contribution from the PVdF in the electrode. The contribution from PVdF calculated from the weight ratio of the electrode was approximately F/V = 0.407. In all the samples, an F/V ratio exceeding this value was detected from the surface even after a long etching time, suggesting that CaF_2 was
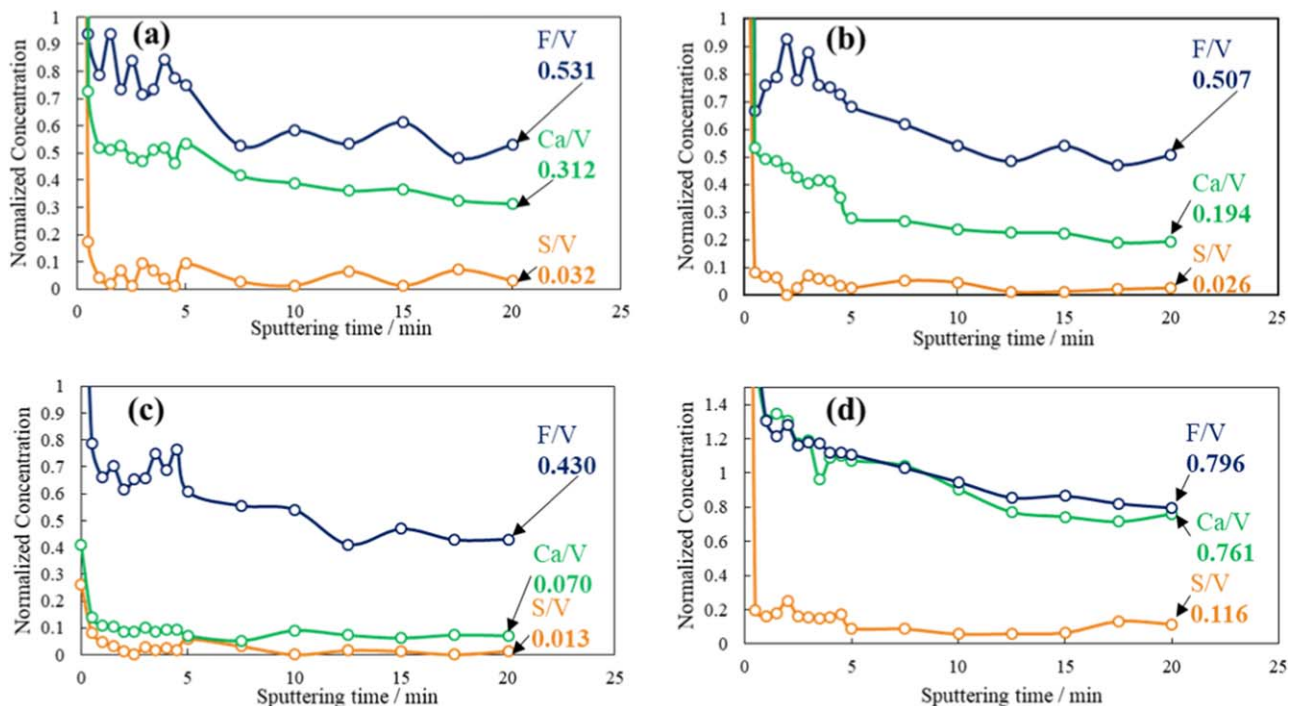
Figure 9. Quantitative elemental analysis by XPS in the depth direction of the electrode cycled in (a) 0.5 M EC:DMC, (b) 0.3 M EC:DMC, (c) 0.5 M G3, and (d) 0.5 M AN.

formed as a surface film. Although, CaF_2 appeared to remain dominant in the F1s spectra even though the F/V ratio was 0.430 after sufficient etching when 0.5 M G3 was used (Fig. S7). This suggests that PVdF may have been damaged and decomposed during etching. Conversely, the elemental quantitative ratios that are higher than the values calculated from the electrode composition can be considered as the contribution from the surface film, that is, the information reflecting the thickness of the surface film. A comparison of the samples showed that a large difference depending on the electrolyte lies in the concentration of the elements other than vanadium (F, Ca, and S) in the decomposition products. Therefore, the concentration at the depth etched with Ar^+ for 20 min decreased with the CIPs. This corresponded to a decrease in the film thickness due to a decrease in the CIPs and an improvement in the electrochemical performance.

Conclusions

We investigated the electrolyte structure using various organic solvent species and salt concentrations, and we clarified the dependency of the electrochemical performance of V_2O_5 nanosheet cathode materials on the electrolyte. The result of a structural analysis of the electrolytes by Raman spectroscopy revealed that the Ca^{2+}-$TFSI^-$ CIP ratio changes according to the solvent species, which are in the following order: G3 < PC < EC:PC < EC:DMC < AN < G1. The CIP ratio decreased as the polarity of the solvent increased. However, in 0.5 M G3, the CIP reduced despite the low polarity of G3. Furthermore, a large molar ratio of CIPs was confirmed in G1 with similar polarities and small solvent sizes. This is because the solvation of G3 surrounding Ca^{2+} separates $TFSI^-$ and Ca^{2+}, thereby forming SSIPs. From the results of the electrochemical tests, the CIP state is directly related to the performance of V_2O_5, such as the capacity and rate performance. In contrast, 0.5 M G3 does not have good coulombic efficiency despite its low CIP ratio. As a factor of the electrolyte instability when 0.5 M G3 was used, Ca^{2+} $(G3)_n$ $TFSI^-$ SSIP was as reductively unstable as the CIPs. The results of the elemental analysis in the depth direction showed that there were elemental species derived from $TFSI^-$. This implies the deposition of a surface film owing to the decomposition of the CIPs. Moreover, the surface film becomes thinner as the ion CIP ratio decreases. This

shows good electrochemical performance and indicates that the charge transfer process by the formed surface film has a strong effect on the electrochemical performance. The coulombic efficiency for 0.5 M G3 indicated numerous side reactions, but the surface film was very thin. This suggests that the product is soluble in the electrolyte, or a film containing no Ca is formed. The electrolyte with a certain degree of CIP has better coulombic efficiency after the cycles due to the stabilization of the electrochemical reaction. From this viewpoint, 0.3 M EC: DMC has well-balanced cycle stability and rate performance. These findings show that ion pairing is very important in the design of the electrolytes for CIBs. However, there is still room for improvement in electrolyte stability, as can be seen from the poor coulombic efficiency. As a specific solution, it is necessary to study alternative anion species.

ORCID

Yoshiaki Murata https://orcid.org/0000-0001-5586-0401

References

1. A. Ponrouch, C. Forntera, F. Bardé, and M. R. Palacín, *Nat. Mater.*, **15**, 169 (2016).
2. M. Hayashi, H. Arai, H. Ohtsuka, and Y. Sakurai, *J. Power Sources*, **119**, 617 (2003).
3. Y. Murata, S. Takada, T. Obata, T. Tojo, R. Inada, and Y. Sakurai, *Electrochim. Acta*, **294**, 210 (2019).
4. Y. Murata, R. Minami, S. Takada, K. Aoyanagi, T. Tojo, R. Inada, and Y. Sakurai, *AIP Conf. Proc.*, **1807**, 020005 (2017).
5. A. L. Lipson, S. Kim, B. Pan, C. Liao, T. T. Fister, and B. J. Ingram, *J. Power Sources,*, **369**, 133 (2017).
6. T. Tojo, Y. Sugiura, R. Inada, and Y. Sakurai, *Electrochim. Acta*, **207**, 22 (2016).
7. N. Kuperman, P. Padigi, G. Goncher, D. Evans, J. Thiebes, and R. Solanki, *J. Power Sources*, **342**, 414 (2017).

8. P. Padigi, G. Goncher, D. Evans, and R. Solanki, *J. Power Sources*, **273**, 460 (2015).

9. T. Shiga, H. Kondo, Y. Kato, and M. Inoue, *J. Phys. Chem. C*, **119**, 27946 (2015).

10. A. L. Lipson, B. Pan, S. H. Lapidus, C. Liao, J. T. Vaughey, and B. J. Ingram, *Chem. Mater.*, **27**, 8442 (2015).

11. D. S. Tchitchekova, A. Ponrouch, R. Verrelli, T. Broux, C. Frontera, A. Sorrentino, F. Bardé, N. Biskup, M. E. A. Dompablo, and M. R. Palacín, *Chem. Mater.*, **30**, 847 (2018).

12. M. Wang, C. Jiang, S. Zhang, X. Song, Y. Tang, and H.-M. Cheng, *Nat. Chem.*, **10**, 667 (2018).

13. S. J. R. Prabakar, A. B. Ikhe, W. B. Park, K.-C. Chung, H. Park, K.-J. Kim, D. Ahn, J. S. Kwak, K.-S. Sohn, and M. Pyo, *Adv. Sci.*, **6**, 1902129 (2019).

14. A. Shyamsunder, L. E. Blanc, A. Asssoud, and L. F. Nazar, *ACS Energy Lett.*, **4**, 2271 (2019).

15. Z. Li, O. Fuhr, M. Fichtner, and Z. Z. Karger, *Energy Environ. Sci.*, **12**, 3496 (2019).

16. S. Gheytani, Y. Liang, F. Wu, Y. Jing, H. Jing, H. Dong, K. K. Rao, X. Chi, F. Fang, and Y. Yao, *Adv. Sci.*, **4**, 1700465 (2017).

17. H. Song, C. Zhang, Y. Liu, C. Liu, X. Nan, and G. Cao, *J. Power Sources*, **294**, 1 (2015).

18. D. S. Tchitchekiva, D. Monti, P. Johansson, F. Bardé, A. R. Vitanova, M. R. Palcín, and A. Ponrouch, *J. Electrochem. Soc.*, **164**, A1384 (2017).

19. T. Mandai, K. Tatesaka, K. Soh, H. Masu, A. Choudhary, Y. Tateyama, R. Ise, H. Imai, T. Takeguchi, and K. Kanamura, *Phys. Chem. Chem. Phys.*, **21**, 12100 (2019).

20. T. Watkins and D. A. Buttry, *J. Phys. Chem. B*, **119**, 7003 (2015).

21. A. V. Cresce et al., *Phys. Chem. Chem. Phys.*, **19**, 574 (2017).

22. D. M. Seo, O. Borodin, S.-D. Han, P. D. Boyle, and W. A. Henderson, *J. Electrochem. Soc.*, **159**, A1489 (2012).

23. Y. Chernyak, *J. Chem. Eng. Data*, **51**, 416 (2006).

24. F. Cataldo, *Eur. Chem. Bull.*, **4**, 92 (2015).

25. R. Naejus, D. Lemordant, R. Coudert, and P. Willman, *J. Chem. Thermodyn.*, **29**, 1503 (1997).

26. J. R. Partington and E. G. Cowley, *Nature*, **135**, 474 (1935).

27. L. G. Gagliardi, C. B. Castells, C. Ràfols, M. Rosés, and E. Bosch, *J. Chem. Eng. Data*, **52**, 1103 (2007).

28. S. Tang and H. Zhao, *RSC Adv.*, **4**, 11251 (2014).

29. Q. Zou and Y.-C. Lu, *J. Phys. Chem. Lett.*, **7**, 1518 (2016).

30. R. Richert, *J. Phys.: Condens. Matter*, **8**, 6185 (1996).

31. T. Koketsu et al., *Nat. Mater.*, **16**, 1142 (2018).